



OPEN

SUBJECT AREAS:

LABORATORY
TECHNIQUES AND
PROCEDURES

STRUCTURAL PROPERTIES

SYNTHESIS AND PROCESSING

Received

27 October 2014

Accepted

2 January 2015

Published

28 January 2015

Correspondence and
requests for materials
should be addressed to
I.-D.K. (jdkim@kaist.
ac.kr)

Highly Efficient Electronic Sensitization of Non-oxidized Graphene Flakes on Controlled Pore-loaded WO₃ Nanofibers for Selective Detection of H₂S Molecules

Seon-Jin Choi¹, Chanyong Choi², Sang-Joon Kim¹, Hee-Jin Cho¹, Meggie Hakim³, Seokwoo Jeon² & Il-Doo Kim¹

¹Department of Materials Science and Engineering, Korea Advanced Institute of Science and Technology, 291 Daehak-ro, Yuseong-gu, Daejeon 305-701, Republic of Korea, ²Department of Materials Science and Engineering and Graphene Research Center of KI for the NanoCentury, Korea Advanced Institute of Science and Technology, Daejeon 305-701, Republic of Korea, ³Platforms Engineering Group, Intel Corporation, Haifa 31015, Israel.

Tailoring of semiconducting metal oxide nanostructures, which possess controlled pore size and concentration, is of great value to accurately detect various volatile organic compounds in exhaled breath, which act as potential biomarkers for many health conditions. In this work, we have developed a very simple and robust route for controlling both the size and distribution of spherical pores in electrospun WO₃ nanofibers (NFs) via a sacrificial templating route using polystyrene colloids with different diameters (200 nm and 500 nm). A tentacle-like structure with randomly distributed pores on the surface of electrospun WO₃ NFs were achieved, which exhibited improved surface area as well as porosity. Porous WO₃ NFs with enhanced surface area exhibited high gas response ($R_{\text{air}}/R_{\text{gas}} = 43.1$ at 5 ppm) towards small and light H₂S molecules. In contrast, porous WO₃ NFs with maximized pore diameter showed a high response ($R_{\text{air}}/R_{\text{gas}} = 2.8$ at 5 ppm) towards large and heavy acetone molecules. Further enhanced sensing performance ($R_{\text{air}}/R_{\text{gas}} = 65.6$ at 5 ppm H₂S) was achieved by functionalizing porous WO₃ NFs with 0.1 wt% non-oxidized graphene (NOGR) flakes by forming a Schottky barrier ($\Delta\phi = 0.11$) at the junction between the WO₃ NFs ($\phi = 4.56$ eV) and NOGR flakes ($\phi = 4.67$ eV), which showed high potential for the diagnosis of halitosis.

Semiconductor metal oxides (SMOs) have attracted tremendous attention as building blocks in chemical sensors due to the distinctive resistivity changing features in a certain ambient, which stimulates many researchers to develop highly sensitive and selective sensors for applications in environmental monitoring^{1,2} and diagnostic analysis³. An extensive amount of research has been done to develop novel synthetic processes to obtain highly porous SMO nanostructures with increased surface area, thereby leading to enhanced surface reaction sites and gas transport in sensing layers^{4,5}. The electrospinning approach is identified as one of the most facile and versatile routes for producing one-dimensional (1D) SMOs structures with high a surface-to-volume ratio exhibiting enhanced porosity^{6,7}. For example, SMO nanofibers (NFs) assisted by a hot-pressing step^{8,9} could generate bimodal pore distribution after the thermo-compression of metal precursor/polymer composite NFs followed by calcination. Phase separation^{10,11} between inorganic precursors and polymers within electrospun metal precursor/polymer composite NFs, which induces open porosity, i.e., elongated pores aligned to fiber direction, in SMO NFs after the decomposition of a polymer-rich region, leading to superior sensitivity toward analytes. In addition, polymeric nanofiber as a sacrificial template combined with physical/chemical vapor deposition of thin SMOs layers, followed by high temperature calcination, produces open tubular structures due to the thermal decomposition of inner polymeric fibers^{12,13}. These morphologies facilitate gas penetration through open pores and also enable an enhanced surface reaction. So far, several types of sacrificial templates such as polyacrylic acid (PAA), polyvinyl alcohol (PVA), polyvinylpyrrolidone (PVP) and mineral oil have been



adopted in the electrospinning processes to prepare the porous metal, metal oxide, polymeric and carbon NF structure with the controlled pore size and density^{14–16}. For example, Lee *et al.* and Jo *et al.* reported polymeric polyacrylonitrile (PAN) fibers with linked pores, which were synthesized by spherical polymethyl methacrylate (PMMA) colloid templates^{17,18}. In addition, Tran *et al.* also proposed porous carbon NFs with distributed mesopores (2–4 nm) using Nafion sacrificial templates¹⁹. However, most materials are based on 1D polymers and carbons, whereas electrospun SMO NFs assisted by polymeric colloid templates have not yet been demonstrated. In particular, the creation of bimodal-pore distribution including both mesoscale and macroscale pores with controlled size and density has hardly been studied in SMO structures.

Besides the manipulation of surface area and porosity of SMO nanostructures, catalytic sensitization on nanostructured SMOs has been identified as an effective method to improve the sensing response as well as selectivity. Typically, noble metals, which are synthesized as nanoparticles, such as Pt¹⁰, Pd²⁰, and Ag²¹, are examples of catalytic sensitizers functionalized on an SMO. More recently, SMOs functionalized with graphene-based materials have attracted a great deal of attention for the enhanced environmental hazardous monitoring and exhaled breath analysis^{22–24}. We have previously demonstrated the high sensitivity and selectivity of thin graphite- and graphene oxide-loaded WO₃ hemitube composites toward hydrogen sulfide (H₂S) and acetone (CH₃COCH₃)²⁵, as well as reduced graphene oxide nanosheet-loaded SnO₂ NF composites²⁶ for potential application in diagnosis of halitosis and diabetes. Noticeably enhanced sensing performance in graphene-functionalized SMO composites were observed, which was attributed to the sensitization effect of graphene-based materials. However, most of the work was performed using chemically modified graphene²⁷ or (reduced) graphene oxide²⁸ for the preparation of graphene-functionalized SMO composites. In addition, gas sensing characteristics using electrospun SMO NFs functionalized with non-oxidized graphene (NOGR) flakes have not been investigated.

Here, we demonstrated for the first time, the facile manipulation of bimodal pore size and density in WO₃ NFs *via* a spherical polystyrene (PS) colloidal templating route. In addition, remarkably improved sensing response and superior selectivity were achieved by functionalizing NOGR flakes on the controlled pore-loaded WO₃ NFs. The potential use of the porous WO₃ NF-NOGR composites for selective H₂S detection against other interfering gases for the accurate diagnosis of halitosis is discussed.

Results

Pore Size and Pore Distribution Control in WO₃ NFs. A schematic illustration for obtaining porous WO₃ NFs using spherical PS

colloids and the composite of NOGR-loaded porous WO₃ NFs is shown in Figure 1. The nonwoven WO₃ NFs can be obtained by a conventional single nozzle electrospinning of the W precursor (ammonium metatungstate hydrate)/PVP composite solution followed by high-temperature calcination. During the preparation of the electrospinning solution, insoluble PS colloids were added and dispersed homogeneously within composite electrospinning solution. After the electrospinning, the spherical PS colloids were decorated on the surface as well as embedded in the W precursor/PVP composite NFs (Figures 1a and b). The spherical PS colloids and the PVP were eliminated, and W precursor was oxidized to form WO₃ NFs during the high-temperature calcination process. A distinctive morphological uniqueness indicated that the spherical pores on the surface as well as inside of the WO₃ NFs were generated as a result of the decomposition of the spherical PS colloids (Figure 1c). It is advantageous that the pore size and the distribution can be controlled in WO₃ NFs by using different sizes of PS colloids in the electrospinning solution, which will provide better gas-sensing performance by increasing surface area and, thus, facilitating the gas penetration path through the pores. In addition, the sensitization effect of NOGR flakes can further enhance the sensing characteristics when the porous WO₃ NFs are functionalized with NOGR flakes (Figure 1d).

Microstructural and morphological observation was performed for the porous WO₃ NFs synthesized by electrospinning assisted by spherical PS colloid sacrificial templates as well as for pristine WO₃ NFs for comparison purposes (Figure 2). Two different sizes of spherical PS colloids having uniform diameters (i.e. average 200 nm and 500 nm) were used during the electrospinning process (Supporting Information, Figure S1). The as-spun W precursor/PVP composite NFs without PS colloid templates showed smooth surfaces (Figure 2a), whereas rough and rugged surface morphology was observed in the case of the PS colloid template assisted W precursor/PVP composite NFs with an average diameter of $1.29 \pm 0.48 \mu\text{m}$ (Figures 2b and c). The spherical PS colloids with uniform size (500 nm in diameter) were well-distributed within the W precursor/PVP composite NFs (Figure 2b). In addition, two different spherical PS colloids were successfully decorated and embedded in the W precursor/PVP composite NFs (Figure 2c). After calcination in air at 500°C, polymeric components, i.e., PS colloids and PVP, were decomposed and burned out, and W precursor was crystallized into WO₃ NFs. The pristine WO₃ NFs showed densely packed polycrystalline microstructures exhibiting smooth surface morphology (Figure 2d) (hereafter, the pristine WO₃ NFs are referred to dense WO₃ NFs). However, porous WO₃ NFs, obtained by spherical PS colloid templates, having diameters of $633 \pm 178 \text{ nm}$, exhibited several pores on the surface and rugged surface morphology

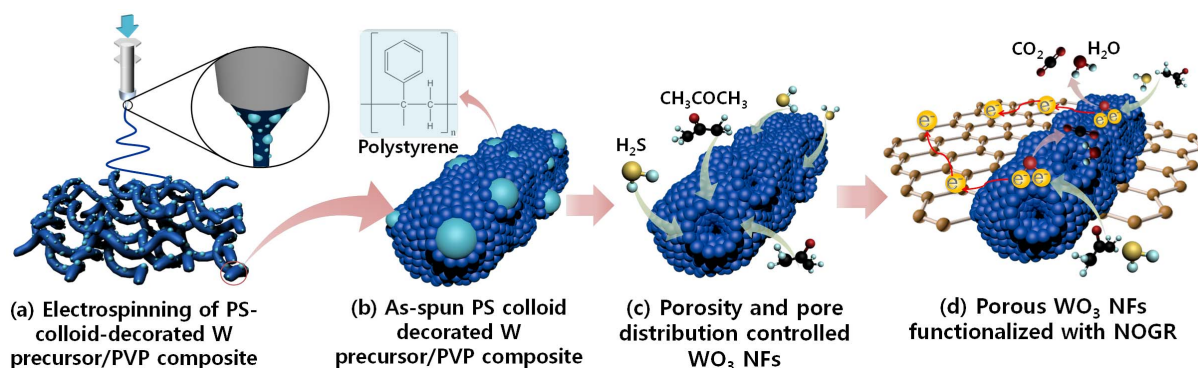


Figure 1 | Schematic illustration of synthetic process for the porous WO₃ NFs: (a) Electrospinning of the spherical PS-colloid-decorated W precursor/PVP composite NFs, (b) detailed description of the spherical PS-colloid-decorated W precursor/PVP composite NFs, (c) pore size and pore distribution controlled WO₃ NFs obtained after high-temperature calcination, (d) sensitizing effect of non-oxidized graphene flake functionalized porous WO₃ NFs.

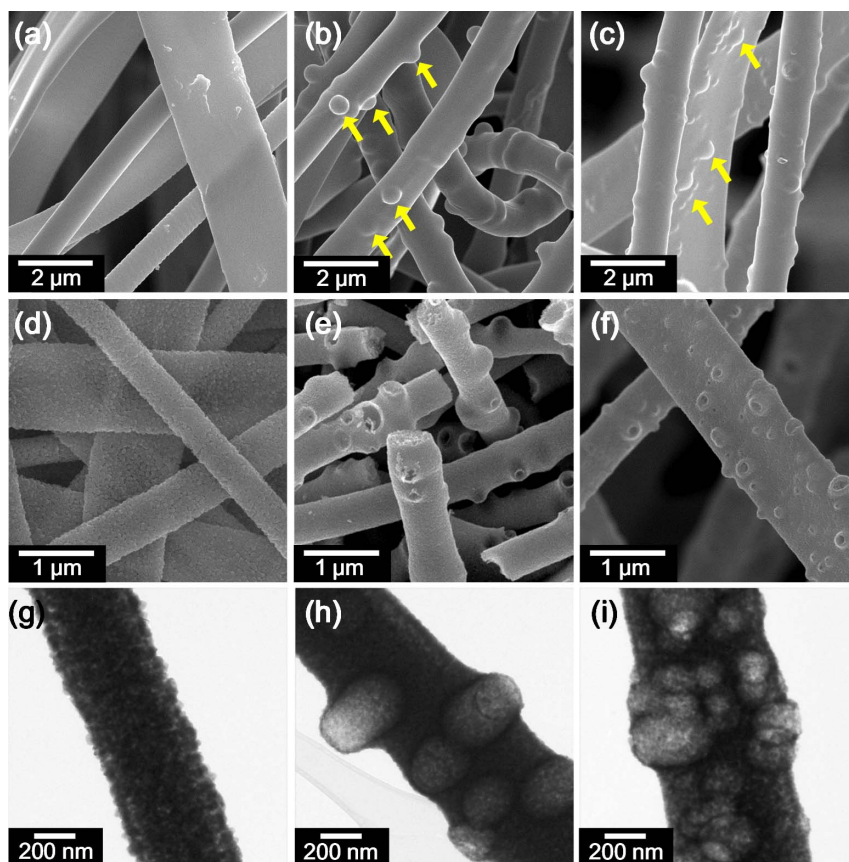


Figure 2 | SEM images of electrospun WO_3 NFs: (a) as-spun dense W precursor/PVP composite NFs, (b) as-spun W precursor/PVP composite NFs embedded with 500 nm PS colloids, (c) as-spun W precursor/PVP composite NFs embedded with 200 nm and 500 nm PS colloids, (d) calcined dense WO_3 NFs, (e) calcined PS (500)- WO_3 NFs, and (f) calcined PS (200&500)- WO_3 NFs. TEM images of electrospun WO_3 NFs: (g) calcined dense WO_3 NFs, (h) calcined PS (500)- WO_3 NFs, and (i) calcined PS (200&500)- WO_3 NFs.

(Figures 2e and 2f) (hereafter, the porous WO_3 NFs synthesized by PS colloids having 500 nm in diameter are referred to PS (500)- WO_3 NFs). The PS (500)- WO_3 NFs exhibited a tentacle-like structure with a crater-like pore shape on the surface. A wider distribution range in pore sizes was achieved in the porous WO_3 NFs synthesized by the two different PS colloids (Figure 2f) (hereafter, the porous WO_3 NFs synthesized by two different PS colloids having diameters of 200 nm and 500 nm are referred to PS (200&500)- WO_3 NFs). To investigate the pore size and the distribution in detail, transmission electron microscopy (TEM) analysis was performed (Figures 2g-i and Figure S2 in the Supporting Information). The dense WO_3 NF, which was composed of closely packed small WO_3 grains exhibiting diameters of approximately 25 nm (Figure 2g), showed the diameter of average 767 ± 325 nm. In contrast, large spherical pores were observed with the PS (500)- WO_3 NFs (Figure 2h) and PS (200&500)- WO_3 NFs (Figure 2i). In particular, larger numbers of spherical pores were interconnected with each other in the case of PS (200&500)- WO_3 NFs. It is noted that the 40–60% reduction in pore sizes were observed after calcination, compared to the original size of the PS colloids. This feature is mainly attributed to the shrinkage of the spherical PS colloids during the thermal decomposition and the migration of W precursor in the early stage of heat treatment. Different pore sizes could be also obtained by varying the PS colloidal sizes, i.e., 100 nm and 200 nm (Supporting Information, Figure S2). It was revealed that WO_3 NFs with pore sizes smaller than 50 nm were obtained by using the PS colloids having diameter of 100 nm due to the shrinkage of the PS colloids (Supporting Information, Figures S2a and b). Thus, the utilization of PS colloids with broad size distribution can lead to effective manipulation of the pore sizes. These results revealed that the pore size (from mesopore to macro-

pore size) and the distribution in 1D metal oxide NFs can be easily controlled for a specific application by simply changing the size and the density of sacrificial colloidal templates.

To evaluate the pore generation behavior during the calcination process, thermal gravimetric analysis (TGA) was performed with the samples of W precursor/PVP composite NFs and PS colloids embedded W precursor/PVP composite NFs (denoted as W precursor/PVP/PS) (Figure 3). Similar weight loss curves were observed in both samples, which showed sharp weight loss (approximately 25% loss) in the temperature range of 220–325°C and entire decomposition of organic compounds above 550°C. To confirm the decomposition temperature of the PS colloids, differential thermal gravimetric (DTG) curves of each sample were compared. The distinctive difference was observed in the temperature range of 325–390°C (red box), in which the range was considered to be the decomposition temperatures of the PS colloids. This observation is consistent with a previous study in which the PS decomposition temperatures were in the range of 200–450°C²⁹. In the case of PVP, it was reported that the decomposition occurs in the temperature range of 350–470°C³⁰. The onset decomposition temperature (350°C) of PVP was identical with our observation but a slightly higher burnout temperature was observed (550°C) (blue box), which is ascribed to the interaction between PVP and W precursor/PS colloid in the as-spun composite NFs. It was concluded that the pores can be generated by the co-decomposition of the PS colloids and the PVP during the calcination process while transforming of W precursor into WO_3 . In addition, the spherical pore structure was attributed to the transformation of the PS colloid domains into void domains after the removal of the spherical PS colloids. The shrunk pore size can be explained by the fact that the higher decomposition temperature of PVP is attributed to the clog-

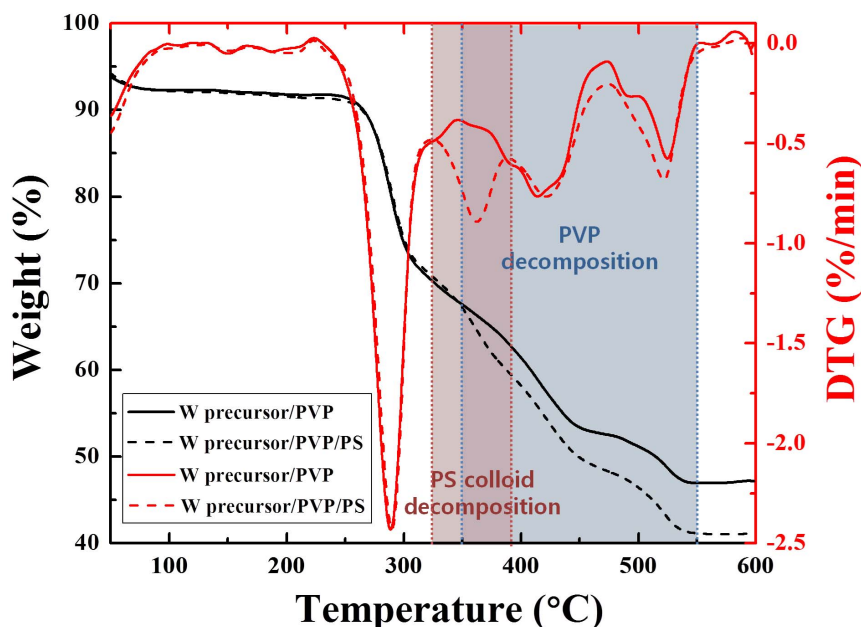


Figure 3 | Thermal gravimetric analysis (TGA) and differential thermal gravimetric (DTG) analysis of the W precursor/PVP composite NFs and W precursor/PVP/PS composite NFs in the temperature range of 30–600 °C.

ging of the pores above 390 °C after complete decomposition of the PS colloids as well as the migration of W precursor into the pore at high temperatures.

To investigate the pore structure and pore distribution, magnified TEM images were analyzed (Supporting Information, Figure S3). Basically, the spherical PS colloids were randomly distributed along the fibers during electrospinning and converted into pores after calcination (Figure S3a). Single PS colloid can be embedded at the inside of the WO₃ NFs, and several PS colloids can be clustered by forming linked pores (Figures S3b and c). In addition, pores were connected from the surface to the inside of the WO₃ NFs by parallel linking of the spherical PS colloids (Figure S3d). It was interesting to note that two distinctive differences in pore structures, which were formed near the surface of the WO₃ NFs, were observed. One was the closed pore at the surface, which contributes to the rough surface morphology of the WO₃ NFs (Figure S3e). The closed pores can be obtained by the PS colloids covered by W precursor on the surface, which resulted in the formation of thin WO₃ layers after the calcination. The other type was open pore structure, in which the structure was similar to a crater (Figure S3f). The formation mechanism of the open pores was regarded to be that either barely coated or uncoated PS colloids by W precursor can be transformed into crater-like pores after the calcination. The open pores and linked pores are particularly advantageous for the gas sensing characteristic considering the enhanced gas penetration as well as the increased surface area to react with gas molecules¹⁰.

High-resolution TEM (HRTEM) analysis was performed to investigate crystallographic structures (Figure 4). The analysis was performed on the extruded pore site at the surface of the porous WO₃ NFs (Figure 4a). The magnified TEM image (dotted red box) revealed that the synthesized porous WO₃ NFs exhibited highly crystallized monoclinic structure with interplanar distances of 3.85 Å, 2.67 Å, and 3.75 Å, which correspond to the crystal planes of (002), (202), and (020) (Figure 4b). Selected area electron diffraction (SAED) patterns of the porous WO₃ NFs were investigated in which the (020), (022), and (411) crystal planes, which correspond to the interplanar distances of 3.75 Å, 2.71 Å, and 1.72 Å, were observed (Figure 4c).

Synthesis of Porous WO₃ NFs Functionalized by Non-oxidized Graphene Flakes.

Highly conducting non-oxidized graphene

(NOGR) flakes exfoliated from a graphite intercalation compound (GIC) were used to enhance the overall conduction of the WO₃ NFs, and the detailed synthesis method of the flakes was reported elsewhere (see Methods Section)^{31–34}. The porous WO₃ NF-NOGR composite was achieved by simply mixing the two solutions, i.e., the porous WO₃ NF dispersed in ethanol and the NOGR flakes dispersed in acetone.

The composite of PS (500)-WO₃ NFs with 0.1 wt% NOGR flakes were investigated by TEM (Figures 4d–f). The NOGR flakes, which were prepared with 1–6 layers, were attached to the porous WO₃ NF, as shown in Figure 4d. The magnified image of Figure 4d (red solid box) revealed that the thin layer of NOGR flakes was well-decorated on the porous WO₃ NF (Figure 4e). The physical contact by anchoring the two-dimensional structure of NOGR flakes on the porous WO₃ NFs can lead to the functionalization of several WO₃ NFs (Supporting Information, Figure S4). The characteristic SAED pattern was obtained with the composite of PS (500)-WO₃ NFs with 0.1 wt% NOGR flakes, which showed the hexagonal pattern of a crystallite graphene structure³⁵ (Figure 4f).

Microstructure and Chemical Analysis of Porous WO₃ NF-NOGR Composite.

The microstructure and chemical state were investigated with the dense WO₃ NFs, PS (200&500)-WO₃ NFs, and PS (500)-WO₃ NFs functionalized with 0.1 wt% NOGR flakes. X-ray diffraction (XRD) analysis revealed that several crystal planes were identified with the three samples in which the characteristic peaks of (020), (002), (200), (012), (021), (120), (022), (202), and (202) were observed (Supporting Information, Figure S5), which were partially observed in the HRTEM analysis and SAED pattern in Figures 4b and c. The crystallographic structure of WO₃ NFs was confirmed to be monoclinic crystal (JCPDS file no. 43–1035). However, the characteristic peak of NOGR flakes could not be observed in the composite of PS (500)-WO₃ NFs functionalized with 0.1 wt% NOGR flakes, which is assumed to be the detection limit of the trace of NOGR content (0.1 wt%) using the XRD.

To confirm the chemical composition and bonding state of the PS (500)-WO₃ NFs functionalized with 0.1 wt% NOGR flakes, X-ray photoelectron spectroscopy (XPS) analysis was performed (Supporting Information, Figure S6). A survey scan of XPS spectrum confirmed the existence of three components, i.e., W, O, and C

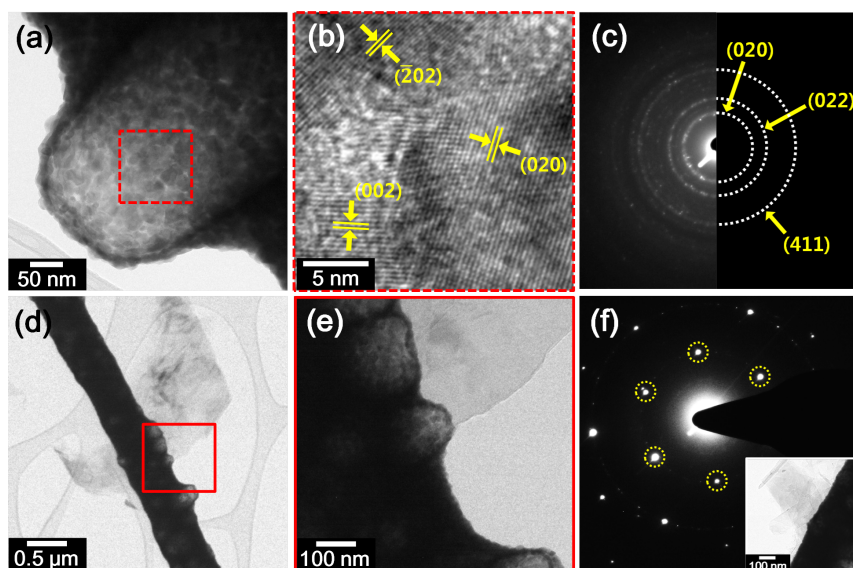


Figure 4 | (a) A TEM image of an extruded pore on the surface of a WO_3 NF, (b) a magnified high-resolution TEM image of a crystallized WO_3 NF (red dotted box in (a)), (c) selected area electron diffraction (SAED) pattern of WO_3 NFs, (d) TEM image of a PS (500)- WO_3 NF functionalized with a 0.1 wt% NOGR flake, (e) magnified TEM image of (d), and (f) SAED pattern of a PS (500)- WO_3 NF functionalized with 0.1 wt% NOGR flakes with a TEM image of an electron beam illuminating the spot shown in the inset.

(Supporting Information, Figure S6a). The high resolution of the XPS spectrum in the vicinity of W $4f$ peaks exhibited two distinctive peaks at the binding energies of 37.6 eV for $4f_{5/2}$ and 35.5 eV for $4f_{7/2}$, which correspond to the typical binding energies of W^{6+} oxidation states (Supporting Information, Figure S6b)³⁶. The characteristic peaks of O $1s$ spectrum were confirmed by O^{2-} and C–OH with binding energies of 530.1 eV and 533.6 eV, respectively (Supporting Information, Figure S6c). Minor peaks of O^- and O_2^- presenting the binding energy of 532.2 eV and 531.4 eV, respectively, were also observed. The dominant peak of O^{2-} as well as minor peaks of O^- and O_2^- were attributed to the adsorption of chemisorbed oxygen species at the surface of WO_3 NFs⁴. The high-resolution spectrum of C $1s$ has a main peak in the vicinity of 284.6 eV, which corresponds to C = C, C – H bonding, as well as one minor peak of C – OH bonding in the vicinity of 286.2 eV (Supporting Information, Figure S6d)³⁷. The chemical analysis with a high-resolution XPS spectrum of carbon is consistent with a previous observation in the literature, which presented by a graphene component³⁸.

Gas-sensing Characteristics. Gas sensing characteristics were investigated with the samples of dense WO_3 NFs, PS (500)- WO_3 NFs, PS (200&500)- WO_3 NFs, and PS(500)- WO_3 NFs functionalized with 0.1 wt% NOGR flakes (referred to NOGR-loaded PS (500)- WO_3 NFs) (Figure 5). The sensing performances toward hydrogen sulfide (H_2S) and acetone (CH_3COCH_3), which are known as biomarkers in exhaled breath for the potential application in diagnosis of halitosis³⁹ and diabetes^{40,41}, were investigated under a highly humid atmosphere (90% RH) to resemble exhaled breath. Firstly, the effects of pore size and pore distribution on the sensing performances were identified at 350°C with a gas concentration in the range of 1–5 ppm (Figures 5a and b). In the case of H_2S sensing, PS (200&500)- WO_3 NFs showed the highest response ($R_{\text{air}}/R_{\text{gas}} = 43.1$ at 5 ppm) compared to that of PS (200)- WO_3 NFs ($R_{\text{air}}/R_{\text{gas}} = 24.1$ at 5 ppm), PS (500)- WO_3 NFs ($R_{\text{air}}/R_{\text{gas}} = 21.2$ at 5 ppm) and dense WO_3 NFs ($R_{\text{air}}/R_{\text{gas}} = 16.4$ at 5 ppm) (Figure 5a and Figure S7a in the Supporting Information). In contrast, PS (500)- WO_3 NFs exhibited the highest response ($R_{\text{air}}/R_{\text{gas}} = 2.8$ at 5 ppm) towards acetone compared to that of dense WO_3 NFs ($R_{\text{air}}/R_{\text{gas}} = 2.3$ at 5 ppm), PS (200&500)- WO_3 NFs ($R_{\text{air}}/R_{\text{gas}} = 2.0$ at 5 ppm), and PS (200)- WO_3 NFs ($R_{\text{air}}/R_{\text{gas}} = 1.4$ at 5 ppm) (Figure 5b and S7b in

the Supporting Information). Secondly, the sensing performance was dramatically improved by functionalization of a small amount (0.1 wt%) of NOGR flakes. The result revealed that PS (500)- WO_3 NFs functionalized with 0.1 wt% NOGR showed the highest response among the sensors toward H_2S ($R_{\text{air}}/R_{\text{gas}} = 65.6$ at 5 ppm) and acetone ($R_{\text{air}}/R_{\text{gas}} = 13.7$ at 5 ppm), which are attributed to the sensitization of NOGR flakes. The sensing characteristics in the temperature range of 200–450°C were investigated to determine the optimum operating temperature, in which the sensors show the highest response towards H_2S and acetone. It was found that the optimum sensitivity was accomplished at 300°C and 350°C for H_2S and acetone, respectively (Supporting Information, Figure S8). At the limit of detection (100 ppb of H_2S or acetone), the relative response ($R_{\text{air}}/R_{\text{gas}}$) of PS (500)- WO_3 NFs functionalized with 0.1 wt% NOGR flakes is 3.9 at 300°C (Figure 5c) and 1.6 at 350°C (Supporting Information, Figure S9). The selectivity of the sensors was examined by exposing the sensor to different analytes (See Methods Section). The results showed high sensitivity to H_2S ($R_{\text{air}}/R_{\text{gas}} = 69.3 \pm 2.5$ at 5 ppm) as well as a noticeable response toward acetone ($R_{\text{air}}/R_{\text{gas}} = 4.4 \pm 0.6$ at 5 ppm) at 300°C maintaining negligible responses ($R_{\text{air}}/R_{\text{gas}} < 2.3$) toward other interfering gases such as toluene ($\text{C}_6\text{H}_5\text{CH}_3$), ethanol ($\text{C}_2\text{H}_5\text{OH}$), nitrogen monoxide (NO), ammonia (NH_3), carbon monoxide (CO), and pentane (C_5H_{12}), which are known as exhaled breath components (Figure 5d).

Discussion

To understand the sensing mechanism depending on the pore size and pore distribution, the base resistance, Brunauer-Emmett-Teller (BET) surface area, and average pore diameters were measured (Figure 6). The base resistances of all the sensors were confirmed, which are closely related with the packing density of the sensing materials⁴². Similar base resistances were observed with dense WO_3 NFs (15.57 M Ω), PS (500)- WO_3 NFs (10.22 M Ω), and PS (200&500)- WO_3 NFs (16.31 M Ω) at an operating temperature of 350°C, which implies that the three sensors have similar packing densities (Figure 6a). The BET surface area and average pore diameter were measured by a surface area analyzer using N_2 vapor. Although dramatic changes were not observed in the BET surface area and average pore diameter, the PS (200&500)- WO_3 NFs exhibited the highest BET surface area (19.22 m²/g) while possessing the

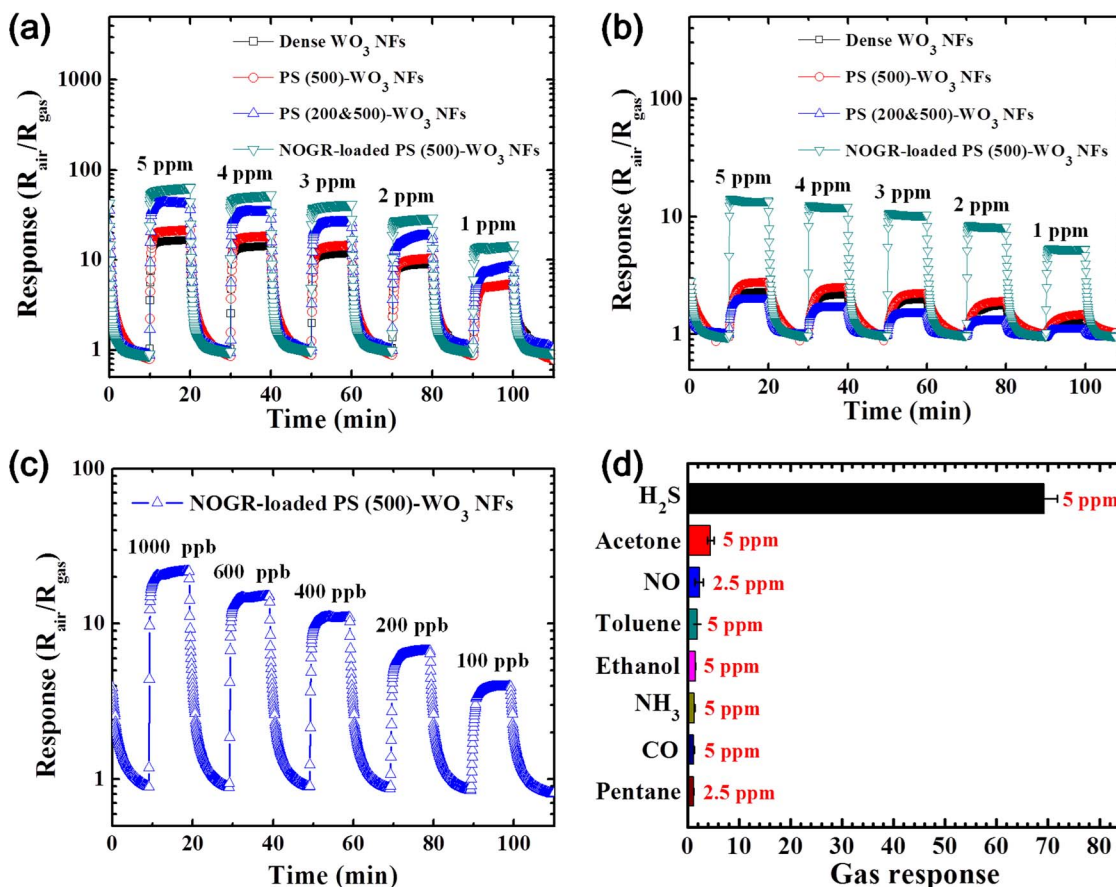


Figure 5 | Gas sensing characteristics of dense WO₃ NFs, PS (500)-WO₃ NFs, PS (200&500)-WO₃ NFs, and PS (500)-WO₃ NFs functionalized with 0.1 wt% NOGR flakes in the gas concentration in the range of 1–5 ppm at 350°C toward (a) H₂S and (b) acetone. (c) Limit of detection of the PS (500)-WO₃ NFs functionalized with 0.1 wt% NOGR flakes toward H₂S down to 100 ppb at 300°C. (d) Selective H₂S detection characteristic of the PS (500)-WO₃ NFs functionalized with 0.1 wt% NOGR flakes with respect to the interfering analytes at 300°C.

lowest average pore diameter (7.98 nm) among the three samples (Figure 6b). In the case of PS (500)-WO₃ NFs, the highest average pore diameter was observed (8.96 nm) with a moderate BET surface area (18.60 m²/g). The dense WO₃ NFs showed the lowest BET surface area (17 m²/g) with a moderate average pore diameter of 8.25 nm. It can be explained that the BET surface area was increased by the pore formation on the surface of WO₃ NFs, in which a higher increase in BET surface area was achieved with the mixture of two different PS colloids (i.e., 200 nm and 500 nm in diameter) than the use of single PS colloids (i.e., 500 nm in diameter). The pore distribution analysis in a mesoscale range of 2–15 nm revealed that both PS (500)-WO₃ NFs and PS (200&500)-WO₃ NFs exhibited higher pore volume compared to the dense WO₃ NFs (Figure 6c). The higher average pore diameter of the dense WO₃ NFs than the PS (200&500)-WO₃ NFs was mainly assumed to be the increased density of pores at the surface of the WO₃ NFs and the formation of the dense WO₃ layer around pores. However, the pore sizes created by the removal of PS colloids must be larger than 30 nm. Therefore, we investigated the macroscale (>50 nm) pore distribution in the range of 50–5000 nm using a porosimeter using Hg (Figure 6d). The result revealed that the higher pore density was observed with the PS (500)-WO₃ NFs and PS (200&500)-WO₃ NFs compared to the dense WO₃ NFs. Similar pore diameters of 678 nm and 677 nm were measured with PS (500)-WO₃ NFs and PS (200&500)-WO₃ NFs, respectively, which were noticeably larger than that (433 nm) of dense PS-WO₃ NFs. Macroscale pores (433 nm), formed in dense PS-WO₃ NFs, are originated from voids between the WO₃ NFs. In the case of PS (200&500)-WO₃ NFs, linked pores, which might be formed by

interconnection between pores formed by PS colloids having different diameters of 200 nm and 500 nm, can contribute to the counting of larger pore sizes. This feature can lead to comparable average pore sizes (677 nm) of PS (200&500)-WO₃ NFs as compared to that (678 nm) of PS (500)-WO₃ NFs by compensating the small pore sizes formed by discrete PS colloids having diameter of 200 nm. However, pore density of PS (200&500)-WO₃ NFs is higher than that of the PS (500)-WO₃ NFs, which is ascribed to the increase in pore density at the surface of the WO₃ NFs by forming linked pores formed by PS colloids having different diameters of 200 nm and 500 nm. The gas sensing characteristics, therefore, can be interpreted to mean that the larger the BET surface, i.e., PS (200&500)-WO₃ NFs, the higher the H₂S sensing performance (Figure 5a), which is attributed to the fact that the small and light molecule of H₂S can penetrate deep into the sensing layers, thereby enhancing the surface reaction between H₂S and chemisorbed oxygen species (O²⁻, O⁻, and O₂⁻). In contrast, large and heavy molecules such as acetone cannot penetrate deep into the sensing layer, which resulted in less of a surface reaction, leading to the lowest acetone response (Figure 5b) to the PS (200&500)-WO₃ NFs having relatively small pore diameter (average 7.98 nm). For this reason, the highest acetone sensing performance was achieved with the PS (500)-WO₃ NFs with an increased pore diameter on the mesoscale (2–50 nm) as well as the macroscale (>50 nm) dimensions, in which the response is controlled by the acetone diffusion into the sensing layers and corresponding surface reaction. This observation is consistent with a previous report using SnO₂ nanoparticle for sensing different analytes^{43,44}. We expect further improvement of gas response *via* the optimization of pore size

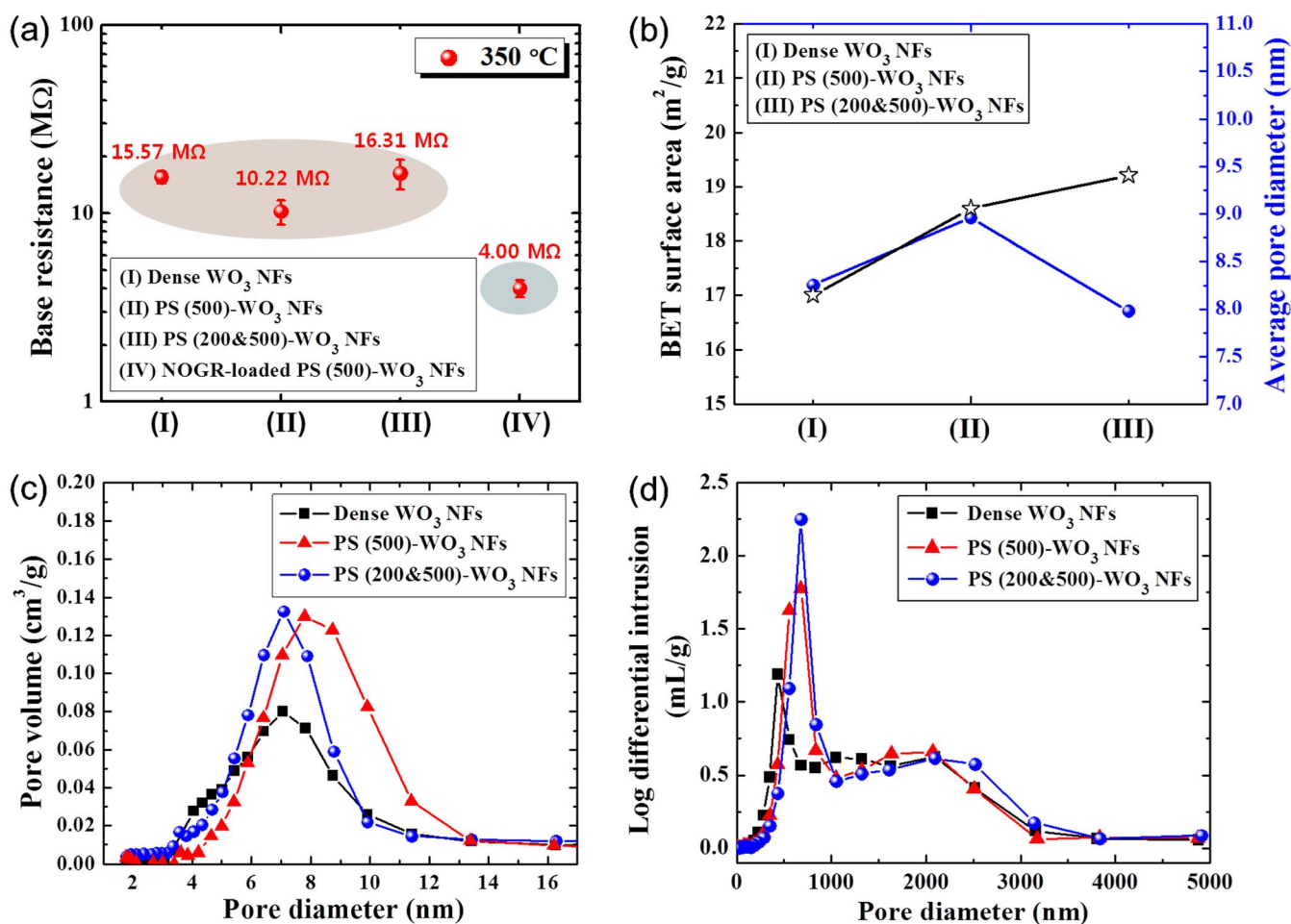


Figure 6 | (a) Base resistance characteristics of dense WO₃ NFs, PS (500)-WO₃ NFs, PS (200&500)-WO₃ NFs, and PS (500)-WO₃ NFs functionalized with 0.1 wt% NOGR at 350 °C, (b) BET surface area and average pore diameter of the dense WO₃ NFs, PS (500)-WO₃ NFs, and PS (200&500)-WO₃ NFs, (c) pore distribution analysis using N₂ vapor in the range of 2–16 nm, and (d) pore distribution analysis using Hg in the range of 3–5000 nm.

and distribution by using PS colloids with various sizes and concentrations.

To explain the significant improvement in sensing performance of the NOGR-loaded WO₃ NFs, we measured the energy band alignment between WO₃ NFs and NOGR flakes using ultraviolet photoelectron spectroscopy (UPS) analysis (Figure 7). The UPS spectrum of PS (500)-WO₃ NFs exhibited a cut-off energy ($E_{\text{cut-off}}$) of 16.64 eV (Figure 7a) and a HOMO energy (E_{HOMO}) of 1.46 eV (in the inset of Figure 7a), indicating that the work function and the electron affinity of the PS (500)-WO₃ NFs are 4.56 eV and 3.22 eV, respectively. The work function of the NOGR flakes was measured using UPS as well, which showed 4.67 eV (Supporting Information, Figure S10); thus, electron transfer from the low work function of PS (500)-WO₃ NFs to the high work function of NOGR flakes can be accomplished by forming a Schottky barrier of 0.11 eV between the junction of NOGR flakes and PS (500)-WO₃ NFs (Figure 7b). Therefore, the improved sensing properties were achieved by the modulating electrons in the WO₃ NFs sensitized by NOGR flakes. The functionalization of NOGR derives the lower electron concentration at the surface of the WO₃ NFs in air, which results in the large conductivity changes upon the exposure of reducing gases such as H₂S and acetone⁴⁵. Nevertheless, the base resistance of the PS (500)-WO₃ NFs functionalized by NOGR flakes (4.00 MΩ) was lower than that (10–16 MΩ) of single phase WO₃ NFs (Figure 6a). In addition, I–V characteristics showed lower the resistance of PS (500)-WO₃ NFs functionalized by NOGR flakes as compared to PS (500)-WO₃ NFs (Supporting

Information, Figure S11). This is attributed to the high electrical conductivity through the NOGR flakes, facilitating charge carrier transport^{25,31}. In addition to the electronic sensitization of NOGR flakes, facile surface reaction process of H₂S with chemisorbed oxygen species^{46,47}, i.e., H₂S (gas) + 3O⁻ (chemisorbed) → SO₂ + H₂O + 3e⁻, generates highly H₂S selective detection.

In this work, facile manipulation of pore size and pore distribution in electrospun WO₃ NFs was firstly demonstrated *via* a polymeric templating route using different sizes of spherical PS colloids (i.e., 200 nm and 500 nm in diameter) as sacrificial templates. During high-temperature calcination step, the co-decomposition of the polymeric components, i.e., PS colloids and PVP, results in the formation of pores by converting the polymeric domains into void domains. In addition, the microstructural and morphological evaluation indicated that different pore structures such as linked, closed, and open pores were observed due to the random distribution of PS colloids in the WO₃ NFs. The gas sensing characteristics revealed that the PS (200&500)-WO₃ NFs showed a significantly enhanced H₂S ($R_{\text{air}}/R_{\text{gas}} = 43.1$ at 5 ppm) response due to the increased BET surface area by an effective surface reaction of the small and light H₂S molecules penetrating through the small pores. In contrast, PS (500)-WO₃ NFs were sensitive to acetone ($R_{\text{air}}/R_{\text{gas}} = 2.8$ at 5 ppm) due to the facile penetration of the large and heavy acetone molecules through the enlarged pores. The synthesized porous WO₃ NFs obtained by PS colloid templates were further integrated with NOGR flakes for the enhanced sensing characteristics. The NOGR

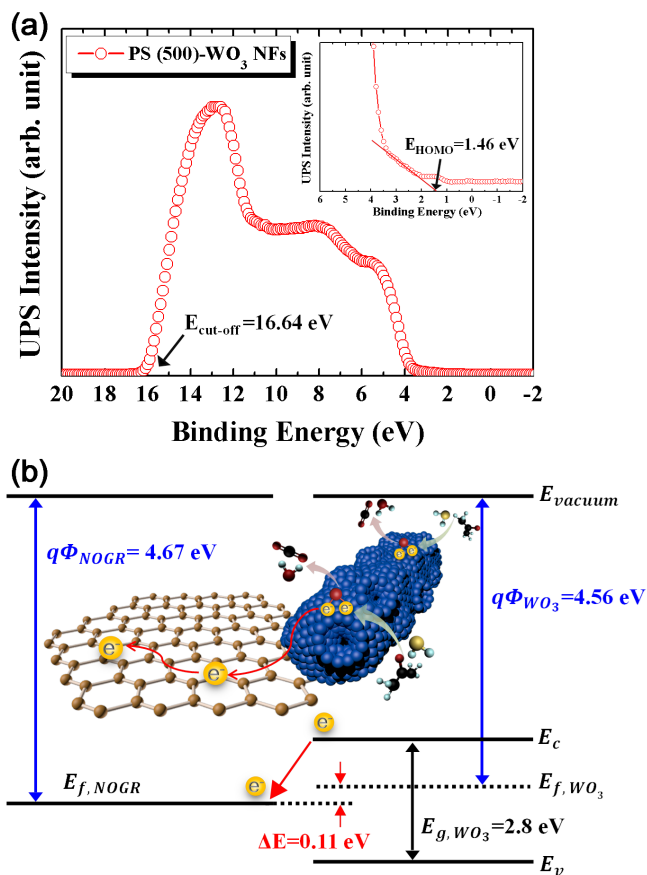


Figure 7 | (a) Ultraviolet photoelectron spectroscopy (UPS) spectrum of PS (500)-WO₃ NFs with a magnified image in the inset, and (b) schematic illustration of the band structure of the NOGR and the PS (500)-WO₃ NFs and electron transport characteristic when the electrical junction is formed.

(0.1 wt%)-loaded PS (500)-WO₃ NFs were highly sensitive to H₂S with a detection limit of 100 ppb ($R_{\text{air}}/R_{\text{gas}} = 3.9$) as well as superior selectivity maintaining minor response ($R_{\text{air}}/R_{\text{gas}} < 2$) to interfering analytes by the electrical sensitization of NOGR. This work verified the effective pore size and pore distribution control method in SMO nanofiber structure as well as the potential use of NOGR flakes without using noble metallic catalysts, which can optimize the sensing characteristics for potential application in diagnosis of halitosis.

Methods

Materials. Ammonium metatungstate hydrate [(NH₄)₆H₂W₁₂O₄₀·xH₂O] and polyvinylpyrrolidone (PVP, M_w = 1,300,000) were purchased from Sigma-Aldrich (St. Louis, USA). 2.5 wt% polystyrene (PS) latex microsphere with diameters of 100 nm, 200 nm and 500 nm, dispersed DI solution was purchased from Alfa Aesar (Ward Hill, USA). All chemicals were used without further purification.

Synthesis of WO₃ NFs with spherical PS colloid templates. To prepare the PS colloid decorated W precursor/PVP solution, 0.2 g of (NH₄)₆H₂W₁₂O₄₀·xH₂O and 0.25 g of PVP were dissolved in 1.5 g of 2.5 wt% polystyrene (PS) latex microsphere dispersed in DI water and continuously stirred at room temperature for 3 h. The electrospinning was performed with the synthesized solution at a feeding rate of 0.1 mL/min using a syringe pump and at a constant DC voltage of 15 kV between the stainless steel foil, employed as a collector, and the syringe needle (21 gauge). The as-spun PS colloid decorated W precursor/PVP composite NFs were calcined at 500 °C for 1 h in air ambient to obtain porous WO₃ NFs. The dense WO₃ NFs were also prepared by the same experimental procedure without the PS colloid dispersion in DI water.

Preparation of non-oxidized graphene (NOGR) flakes. The preparation of NOGR was reported in previous works³¹. Briefly, a ternary eutectic system (KCl (99%, Aldrich), NaCl (99%, Aldrich), and ZnCl₂ (99%, Aldrich)) were used to fabricate graphite intercalation compound (GIC) at 350 °C. The prepared GIC was exfoliated in

a pyridine solution. For fabricating the NOGR flakes, 1-pyrenebutyric acid (20 mg, Aldrich) was added to graphene flakes (20 mg) dispersed in pyridine (40 mL, Aldrich). The mixtures were mildly sonicated for 12 hours and subsequently stored at 70 °C for 24 hours. The mixture was then filtered and washed with DI water using a 0.1 μm-thick Anodic filter to remove salts and residual pyridine. After drying the mixture in a furnace heated to 100 °C, the NOGR flakes (10 mg) were dispersed under sonication in 10 mL of acetone for 3 hours.

Preparation of NOGR-flakes-loaded porous WO₃ NFs composite. The composite of NOGR-flakes-loaded porous WO₃ NFs were obtained by mixing the two dispersed solutions of the NOGR and the WO₃ NFs. For the WO₃ NF solution, 1 mg of PS (500)-WO₃ NFs was dissolved in 100 μL of ethanol. The contents of NOGR flakes in the composite with PS (500)-WO₃ NFs were maintained to be 0.1 wt% to characterize the sensing performance.

Gas sensing characterization. The gas sensing characteristics were evaluated using a measurement setup described elsewhere¹². All of the sensors were stabilized at a highly humid baseline air ambient (90% RH) before the measurement to simulate exhaled breath. The sensors were exposed to different analyte (hydrogen sulfide, nitrogen monoxide, acetone, ammonia, toluene, carbon monoxide, pentane, and ethanol) concentrations ranging from 100 ppb to 5 ppm. Each analyte was exposed for a duration of 10 min followed by 10 min of exposure to air to clean the sensors. The resistance changes were measured using a data acquisition system (34972A, Agilent) and the relative response ($R_{\text{air}}/R_{\text{gas}}$) was measured, where R_{air} is the sensor's baseline resistance upon exposure to air and R_{gas} is the resistance measured upon exposure to the different analytes. The operating temperatures were controlled by applying voltage to the microheater, which was patterned at the back side of the sensor substrate, using a DC power supply (E3647A, Agilent).

- Kim, I. D., Rothschild, A. & Tuller, H. L. Advances and new directions in gas-sensing devices. *Acta Mater.* **61**, 974–1000 (2013).
- Na, C. W., Woo, H. S., Kim, I. D. & Lee, J. H. Selective detection of NO₂ and C₂H₅OH using a Co₃O₄-decorated ZnO nanowire network sensor. *Chem. Commun.* **47**, 5148–5150 (2011).
- Peng, G. *et al.* Diagnosing lung cancer in exhaled breath using gold nanoparticles. *Nat. Nanotechnol.* **4**, 669–673 (2009).
- Yamazoe, N., Sakai, G. & Shimanoe, K. Oxide semiconductor gas sensors. *Catal. Surv. Asia.* **7**, 63–75 (2003).
- Yamazoe, N. Toward innovations of gas sensor technology. *Sens. Actuators B* **108**, 2–14 (2005).
- Lu, X. F., Wang, C. & Wei, Y. One-Dimensional Composite Nanomaterials: Synthesis by Electrospinning and Their Applications. *Small* **5**, 2349–2370 (2009).
- Greiner, A. & Wendorff, J. H. Electrospinning: A fascinating method for the preparation of ultrathin fibres. *Angew. Chem. Int. Edit.* **46**, 5670–5703 (2007).
- Kim, I. D. *et al.* Ultrasensitive chemiresistors based on electrospun TiO₂ nanofibers. *Nano Lett.* **6**, 2009–2013 (2006).
- Kim, I. D. *et al.* Electrospun SnO₂ nanofiber mats with thermo-compression step for gas sensing applications. *J. Electroceram.* **25**, 159–167 (2010).
- Shin, J. *et al.* Thin-Wall Assembled SnO₂ Fibers Functionalized by Catalytic Pt Nanoparticles and their Superior Exhaled-Breath-Sensing Properties for the Diagnosis of Diabetes. *Adv. Funct. Mater.* **23**, 2357–2367 (2013).
- Bognitzki, M. *et al.* Nanostructured fibers via electrospinning. *Adv. Mater.* **13**, 70–72 (2001).
- Choi, S. J. *et al.* Selective Diagnosis of Diabetes Using Pt-Functionalized WO₃ Hemitube Networks As a Sensing Layer of Acetone in Exhaled Breath. *Anal. Chem.* **85**, 1792–1796 (2013).
- Choi, S. H. *et al.* Hollow ZnO Nanofibers Fabricated Using Electrospun Polymer Templates and Their Electronic Transport Properties. *ACS Nano* **3**, 2623–2631 (2009).
- Horzum, N. *et al.* Hierarchically Structured Metal Oxide/Silica Nanofibers by Colloid Electrospinning. *ACS Appl. Mater. & Interfaces* **4**, 6338–6345 (2012).
- Wu, H. *et al.* A transparent electrode based on a metal nanotrough network. *Nat. Nanotechnol.* **8**, 421–425 (2013).
- Li, D. & Xia, Y. N. Direct fabrication of composite and ceramic hollow nanofibers by electrospinning. *Nano Lett.* **4**, 933–938 (2004).
- Lee, S. *et al.* Preparation of macroporous carbon nanofibers with macroscopic openings in the surfaces and their applications. *Nanotechnology* **20**, 445702 (2009).
- Jo, E. *et al.* Core-Sheath Nanofibers Containing Colloidal Arrays in the Core for Programmable Multi-Agent Delivery. *Adv. Mater.* **21**, 968–972 (2009).
- Tran, C. & Kalra, V. Fabrication of porous carbon nanofibers with adjustable pore sizes as electrodes for supercapacitors. *J. Power Sources* **235**, 289–296 (2013).
- Yang, D. J. *et al.* Ultrasensitive and Highly Selective Gas Sensors Based on Electrospun SnO₂ Nanofibers Modified by Pd Loading. *Adv. Funct. Mater.* **20**, 4258–4264 (2010).
- Hwang, I. S. *et al.* Facile Control of C₂H₅OH Sensing Characteristics by Decorating Discrete Ag Nanoclusters on SnO₂ Nanowire Networks. *ACS Appl. Mater. & Interfaces* **3**, 3140–3145 (2011).
- Zhu, Y. W. *et al.* Graphene and Graphene Oxide: Synthesis, Properties, and Applications. *Adv. Mater.* **22**, 5226–5226 (2010).



23. Huang, X. *et al.* Graphene-Based Materials: Synthesis, Characterization, Properties, and Applications. *Small* **7**, 1876–1902 (2011).
24. Huang, Q. W., Zeng, D. W., Li, H. Y. & Xie, C. S. Room temperature formaldehyde sensors with enhanced performance, fast response and recovery based on zinc oxide quantum dots/graphene nanocomposites. *Nanoscale* **4**, 5651–5658 (2012).
25. Choi, S. J. *et al.* Fast Responding Exhaled-Breath Sensors Using WO₃ Hemitubes Functionalized by Graphene-Based Electronic Sensitizers for Diagnosis of Diseases. *ACS Appl. Mater. & Interfaces* **6**, 9061–9070 (2014).
26. Choi, S. J. *et al.* Selective Detection of Acetone and Hydrogen Sulfide for the Diagnosis of Diabetes and Halitosis Using SnO₂ Nanofibers Functionalized with Reduced Graphene Oxide Nanosheets. *ACS Appl. Mater. & Interfaces* **6**, 2588–2597 (2014).
27. Yuan, W. J. *et al.* High-Performance NO₂ Sensors Based on Chemically Modified Graphene. *Adv. Mater.* **25**, 766–771 (2013).
28. Yuan, W. J. & Shi, G. Q. Graphene-based gas sensors. *J. Mater. Chem. A* **1**, 10078–10091 (2013).
29. Peterson, J. D., Vyazovkin, S. & Wight, C. A. Kinetics of the thermal and thermo-oxidative degradation of polystyrene, polyethylene and poly(propylene). *Macromol. Chem. Phys.* **202**, 775–784 (2001).
30. Newsome, T. E. & Olesik, S. V. Electrospinning Silica/Polyvinylpyrrolidone Composite Nanofibers. *J. Appl. Polym. Sci.* **131**, 40966 (2014).
31. Park, K. H. *et al.* Exfoliation of Non-Oxidized Graphene Flakes for Scalable Conductive Film. *Nano Lett.* **12**, 2871–2876 (2012).
32. Ryu, W. H. *et al.* Bifunctional Composite Catalysts Using Co₃O₄ Nanofibers Immobilized on Nonoxidized Graphene Nanoflakes for High-Capacity and Long-Cycle LiO₂ Batteries. *Nano Lett.* **13**, 4190–4197 (2013).
33. Guo, W. M. & Chen, G. H. Fabrication of Graphene/Epoxy Resin Composites with Much Enhanced Thermal Conductivity via Ball Milling Technique. *J. Appl. Polym. Sci.* **131**, 40565 (2014).
34. Kwon, J. *et al.* Simple Preparation of High-Quality Graphene Flakes without Oxidation Using Potassium Salts. *Small* **7**, 864–868 (2011).
35. Hernandez, Y. *et al.* High-yield production of graphene by liquid-phase exfoliation of graphite. *Nat. Nanotechnol.* **3**, 563–568 (2008).
36. Wang, G. M. *et al.* Hydrogen-treated WO₃ nanoflakes show enhanced photostability. *Energ. Environ. Sci.* **5**, 6180–6187 (2012).
37. Yang, D. *et al.* Chemical analysis of graphene oxide films after heat and chemical treatments by X-ray photoelectron and Micro-Raman spectroscopy. *Carbon* **47**, 145–152 (2009).
38. Lv, R. *et al.* Nitrogen-doped graphene: beyond single substitution and enhanced molecular sensing. *Sci. Rep.* **2**, 586 (2012).
39. Tangerman, A. & Winkel, E. G. Extra-oral halitosis: an overview. *J. Breath Res.* **4**, 017003 (2010).
40. Righettoni, M. *et al.* Breath acetone monitoring by portable Si:WO₃ gas sensors. *Anal. Chim. Acta* **738**, 69–75 (2012).
41. Righettoni, M., Tricoli, A. & Pratsinis, S. E. Si:WO₃ Sensors for Highly Selective Detection of Acetone for Easy Diagnosis of Diabetes by Breath Analysis. *Anal. Chem.* **82**, 3581–3587 (2010).
42. Seo, M. H. *et al.* Shimano, K. Microstructure control of TiO₂ nanotubular films for improved VOC sensing. *Sens Actuators B* **154**, 251–256 (2011).
43. Kida, T. *et al.* Pore and Particle Size Control of Gas Sensing Films Using SnO₂ Nanoparticles Synthesized by Seed-Mediated Growth: Design of Highly Sensitive Gas Sensors. *J. Phys. Chem. C* **117**, 17574–17582 (2013).
44. Suematsu, K. *et al.* Nanoparticle Cluster Gas Sensor: Controlled Clustering of SnO₂ Nanoparticles for Highly Sensitive Toluene Detection. *ACS Appl. Mater. & Interfaces* **6**, 5319–5326 (2014).
45. Russo, P. A. *et al.* Room-Temperature Hydrogen Sensing with Heterostructures Based on Reduced Graphene Oxide and Tin Oxide. *Angew. Chem. Int. Edit.* **51**, 11053–11057 (2012).
46. Rout, C. S., Hegde, M. & Rao, C. N. R. H₂S sensors based on tungsten oxide nanostructures. *Sens. Actuators B* **128**, 488–493 (2008).
47. Choi, S. J. *et al.* Facile Au catalyst loading on the inner shell of hollow SnO₂ spheres using Au-decorated block copolymer sphere templates and their selective H₂S sensing characteristics. *Nanoscale* **6**, 11898–11903 (2014).

Acknowledgments

This work was supported by the Center for Integrated Smart Sensors funded by the Ministry of Science, ICT & Future Planning as Global Frontier Project (CISS- 2011-0031870) and Korea Advanced Institute of Science and Technology (KAIST) funded by the Ministry of Science, ICT & Future Planning as End Run Project (N01140506). This research is partially funded by Intel's University Research Office (URO).

Author contributions

S.J.C. and S.J.K. prepared the pore-loaded WO₃ nanofibers using an electrospinning method. C.C. prepared the non-oxidized graphene (NOGR) flakes and analyzed their work function. S.J.C. and H.J.C. characterized the gas sensing properties of WO₃ nanofiber-NOGR composite layers. M.H. and S.J. provided helpful advice during this research work. S.J.C. and I.D.K. analyzed the data and wrote the manuscript. I.D.K. generated the idea and designed the experiments. All authors reviewed the manuscript.

Additional information

Supplementary information accompanies this paper at <http://www.nature.com/scientificreports>

Competing financial interests: The authors declare no competing financial interests.

How to cite this article: Choi, S.-J. *et al.* Highly Efficient Electronic Sensitization of Non-oxidized Graphene Flakes on Controlled Pore-loaded WO₃ Nanofibers for Selective Detection of H₂S Molecules. *Sci. Rep.* **5**, 8067; DOI:10.1038/srep08067 (2015).



This work is licensed under a Creative Commons Attribution-NonCommercial-ShareAlike 4.0 International License. The images or other third party material in this article are included in the article's Creative Commons license, unless indicated otherwise in the credit line; if the material is not included under the Creative Commons license, users will need to obtain permission from the license holder in order to reproduce the material. To view a copy of this license, visit <http://creativecommons.org/licenses/by-nc-sa/4.0/>